A micromechanical-based model of stimulus responsive liquid crystal elastomers

Roberto Brighenti [a,*], Connor G. McMahan [b], Mattia P. Cosma [a], Arda Kotikian [c], Jennifer A. Lewis [c], Chiara Daraio [b]

[a] Dept. of Engineering & Architecture, Univ. of Parma, Viale delle Scienze 181/A, Parma 43124, Italy
[b] Division of Engineering and Applied Science, California Institute of Technology, Pasadena, CA 91125, USA
[c] Paulson School of Engineering and Applied Sciences, Wyss Institute of Biologically Inspired Engineering, Cambridge, MA 02138, USA

ABSTRACT

Stimulus responsive elastomers are advanced engineered materials that perform desired functionalities when triggered by external stimuli. Liquid crystal elastomers (LCEs) are one important example that exhibit reversible actuation when cycled above and below their nematic-to-isotropic transition temperature. Here, we propose a micromechanical-based model that is centered on the evolution of the chain distribution tensor of the LCE network. Our model, framed within the statistical model of the chain network, enables a mesoscale description of their mechanical response under an external thermal stimulus. We compare the model to prior experimental observations of the bending response of 3D printed LCE elements with controlled director alignment.

© 2021 Elsevier Ltd. All rights reserved.

1. Introduction

Several stimulus-responsive polymers have the ability to exert mechanical work when exposed to environmental cues. This has led the materials science community to devote attention to developing, testing, and modeling these materials. As a result, multiple untethered sensors and actuators have been developed for the next generation of soft robots and other shape-morphing applications (Shahinpoor and Schneider, 2008; Aguilar et al., 2007; Schattling et al., 2014; Fu et al., 2018; Guragain et al., 2015; Cao and Wang, 2016). A better understanding of the impact that polymer chemistry has on mechanical properties will allow us to develop new materials that are capable of unprecedented functions.

Liquid crystal elastomers (LCEs) represent an interesting class of responsive polymers that combine mechanical properties of both fluids and solids (Saeva, 1979). Their molecular structure exhibits preferred orientations, akin to liquid crystals (LCs) (De Gennes and Prost, 1993; Warner and Terentjev, 2007). LCs are made of elongated rigid molecules (nematic mesogens) whose preferential orientation is retained in a medium. This orientation can be quantitatively described through a director parameter tensor (Warner and Terentjev, 2007) and the deviation from this average direction is described by the order degree of the mesogens embedded in the polymer network. LCEs are obtained by weakly cross-linking liquid crystal mesogens to a highly deformable elastomeric network (Finkelmann et al., 2001). By combining the deformability of the entropically-dominated elastomeric network with the capacity for reorientation of the nematic mesogens, LCEs can undergo exceptionally large deformations (up to 300–400% with respect to the reference configuration) when an external stimulus induces a phase transformation between their nematic and isotropic states.

The orientation of the nematic mesogens can be manipulated by thermal, electric or magnetic fields, light, and mechanical stimuli (Stephen and Straley, 1974; Terentjev and Warner, 2001; Mitchell et al., 1993). Importantly, the large deformations induced by these external stimuli are reversible and are accompanied by large force or torque outputs. The properties mentioned above make LCEs compelling materials for several applications, including soft robotics, artificial muscles, and deployable structures such as tunable mirrors, to name a few (Kotikian et al., 2019; Ohm et al., 2012).

Multiple fabrication methods have recently been introduced to create LCEs with controlled mesoscale architectures in both two and three dimensions (Surjadi et al., 2019; Ware et al., 2015; Kim et al., 2019; Davidson et al., 2020; Waters et al., 2020; Aharoni et al., 2018; Kowalski et al., 2018; Guin et al., 2018). Of these, 3D printing is perhaps the most flexible method, as it enables local control over the director alignment and composition within 3D LCEs (Kotikian et al., 2018). However, to fully realize the

---

Nomenclature

a_h	Material-dependent parameter defining the spontaneous deformation in LCE
b	Kuhn's length of a chain segment
c_a	Number of active chains per unit volume (chain concentration)
$\boldsymbol{C}_h$	right Cauchy-Green deformation tensor
$\boldsymbol{D} = \left(\boldsymbol{L} + \boldsymbol{L}^T\right)/2$	Symmetric rate of the deformation tensor
E	Young modulus
$\boldsymbol{E}$	Green-Lagrange deformation tensor
$\boldsymbol{F}, F_{ij}, \boldsymbol{F}_h$	Deformation gradient tensor
G	Shear modulus
k_B	Boltzmann constant
$\boldsymbol{L} = \dot{\boldsymbol{F}}\boldsymbol{F}^{-1}, L_{ij}$	Velocity gradient tensor
J	Polymer volume change
$\boldsymbol{n}$	Unit vector defining the nematic order orientation in the 3D space
N	Number of segments in a polymer chain belonging to a single network
$\boldsymbol{P}$	First Piola stress tensor related to the mechanical deformation
$\boldsymbol{Q}, Q$	Nematic order tensor and order parameter of the LCE, respectively
$\boldsymbol{r}$	End-to-end distance of a polymer chain
$\boldsymbol{R}$	Rotation tensor

t	Time
T	Absolute temperature
T_{NI}	Absolute temperature for the LCE phase change
$\varphi_0(\boldsymbol{r}), \varphi(\boldsymbol{r})$	Normalized distribution function of the polymer's chains in the stress-free and in the current state, respectively
φ_{0n}	Normalized distribution function of the material in the initial nematic state (non-isotropic)
$\rho_0(\boldsymbol{r}), \rho(\boldsymbol{r})$	Distribution function of the end-to-end vector in the stress-free and in the current state, respectively
$\boldsymbol{\mu}_0, \boldsymbol{\mu}$	distribution tensor in the initial (stress-free) and in the current state of the polymer, respectively
$\boldsymbol{\mu}_n, \boldsymbol{\mu}_{np}$	Distribution tensor corresponding to the chain distribution function of a nematic network φ_n and its corresponding expression in the principal directions frame of reference, respectively
λ	Stretch of the single polymer chain
ψ	Deformation energy for a single chain
Ψ_0, Ψ	Network's deformation energy per unit volume in the stress-free and in the current configuration, respectively
Ψ_{ext}	Mechanical energy associated to the external forces
π	Hydrostatic pressure
Π	Total potential energy per unit volume of material
$\boldsymbol{\sigma}$	Cauchy stress tensor

---

power of these emerging fabrication methods, there is a need for simulation tools that adequately model their physico-chemical and mechanical behavior and predictively design the desired LCE microstructure to achieve the desired functionality.

Here, we assess the mechanical response of LCE-based elements to thermal stimuli through a quantitative, physics-based micromechanical model. Results from simulations are compared to experimental data from (Kotikian et al., 2019) and to theoretical results from (Agostiniani and DeSimone, 2017). The paper is organized as follows: Section 2 is devoted to illustrating a statistical description of the microstructure of elastomers. In Section 3, we present a mechanical model for LCEs that is based on this statistical approach and we discuss its computational implementation. In Section 4, we comment on the experiments performed in (Kotikian et al., 2019), to which we compare our computational results. We present the numerical simulations and the obtained results in Section 5. Finally, we outline our conclusions and outlook in Section 6.

2. Statistical-based description of LCE mechanics

2.1. Basic concepts

LCEs consist of an amorphous arrangement of entangled linear chains joined at discrete points to form a network, whose behavior can be quantitatively described using a statistical approach. Due to the disordered nature of elastomeric networks, their microstructural state is dominated by entropic energy rather than by the standard enthalpic-like deformation energy typical of crystalline materials. Each chain in a network is usually assumed to be composed of N rigid (Khun's) segments of length b. This arrangement is well described by the random-walk theory (i.e., freely-jointed chain model, or FJC) (Doi, 1996). Upon stretching, the chain elongates, and its entropic energy reduces. However, only finite extensions can take place because the rigidity of the constituting

segments allows for a maximum length of the deformed chain (i.e., the distance between the endpoints of the chain) to be equal to its contour length Nb, corresponding to a maximum stretch limit $\lambda_{max} = \sqrt{N}$.

Based on this concept, the use of a statistical description of the chain distribution within the network is a suitable way of defining the physical state of the polymer. In a stress-free state, the chain end-to-end vectors $\boldsymbol{r}$ can be assumed to be distributed in the 3D space according to the following expression

$$\rho_0(\boldsymbol{r}) = c_a \varphi_0(\boldsymbol{r}) \tag{1}$$

where c_a represents the number of mechanically active chains (i.e. chains joined to the network at both of their extremities), and φ_0 is the normalized distribution function which is usually adopted to be Gaussian. Namely, $\varphi_0(|r|) = \left(\frac{3}{2\pi Nb^2}\right)^{\frac{3}{2}}\exp\left(-\frac{3|r|^2}{2Nb^2}\right)$ (Vernerey et al., 2017). This is characterized by a mean value $\boldsymbol{r} = 0$ and standard deviation $b\sqrt{N/3}$. The integral over the chain configuration space (i.e. the space of all the possible chain lengths and orientations) of the distribution function $\rho_0(\boldsymbol{r})$ provides the number of mechanically active chains:$c_a = \rho_0 = \int_\Omega \langle\rho\rangle_0 \, d\Omega = \int_0^{2\pi} \int_0^\pi \left(\int_0^{Nb} \rho_0(\boldsymbol{r}) \, r^2 dr\right)\sin\theta d\theta d\omega$In the absence of any chain loss (microscopic damage) or gain (such as what occurs in self-healing mechanisms), the number of mechanically active chains must remain constant in time, i.e. $c_a(t) = \langle\rho(t)\rangle = const$. We note that the chain concentration, i.e. the number of fully connected chains per unit volume, is related to the standard shear modulus G of the material through the well-known simple expression $G = c_a k_B T$, where k_B and T are the Boltzmann constant and the absolute temperature, respectively (Doi, 1996).

Statistical descriptions of elastomer mechanics often adopt the affine deformation hypothesis which requires the polymer chains to assume the same deformation of the continuum in which they

are embedded (Kuhn and Grün, 1942). According to the statistical approach, the physical state of the polymer is completely known once the distribution of $\boldsymbol{r}$ is available. Therefore, the knowledge of how the function $\rho(r)$ changes in time suffices to fully determine the mechanical state of the material.

The distribution function $\rho(t)$ evolves in time due to mechanical deformation, the strain rate effect, chain ruptures, chain rearrangement in a transient network, change in the nematic order of a LCE, etc. (Vernerey et al., 2017). Fig. 1 illustrates schematically how the distribution function evolves as a function of deformation.

In polymer physics, the mechanical energy stored in a single chain is usually made to depend on the modulus of the end-to-end vector. According to Gaussian statistics (Rubinstein and Colby, 2003) and for moderate stretch values, the elastic energy of a single chain is given by $\psi(\boldsymbol{r}) = \frac{3k_BT}{2Nb^2}|\boldsymbol{r}|^2$, while the elastic potential energy per unit volume of the polymer is:

$$\Delta\Psi = \Psi - \Psi_0 + A = \int_\Omega [\rho(\boldsymbol{r},t) - \rho_0(\boldsymbol{r})]\psi d\Omega + A$$
$$= c_a\langle[\varphi(\boldsymbol{r},t) - \varphi_0(\boldsymbol{r})]\psi\rangle + \pi[\det(\boldsymbol{F}) - 1]$$
$$= \frac{3c_ak_BT}{2Nb^2}\langle(\varphi - \varphi_0)|\boldsymbol{r}|^2\rangle + \pi[\det(\boldsymbol{F}) - 1] \tag{2}$$

Here, the presence of the difference $\rho(\boldsymbol{r},t) - \rho_0(\boldsymbol{r})$ is justified by the fact that the energy of the polymer is non-zero in its stress-free state. Namely, $\Psi_0 = \langle\rho_0\psi\rangle > 0$ for the distribution ρ_0 corresponding to $\boldsymbol{F} = 1$, where $\boldsymbol{F} = \partial\boldsymbol{x}/\partial\boldsymbol{X} = 1 + \partial\boldsymbol{u}/\partial\boldsymbol{X}$ is the deformation gradient tensor, 1 is the second order identity tensor, and $\boldsymbol{u}$ is the displacement field. Meanwhile, π is the hydrostatic pressure, which serves the role of a multiplier constraint in order to fulfill the incompressibility condition (mathematically expressed by $J = \det(\boldsymbol{F}) = 1$).

By introducing the distribution tensors, $\boldsymbol{\mu}_0 = \langle\varphi_0(\boldsymbol{r}, t = 0)\boldsymbol{r} \otimes \boldsymbol{r}\rangle$, $\boldsymbol{\mu} = \langle\varphi(\boldsymbol{r},t)\boldsymbol{r} \otimes \boldsymbol{r}\rangle$ referred to the initial stress-free and to the current deformed configuration, respectively, the previous energy expression (2) can be rewritten as follows (Vernerey et al., 2017):

$$\Delta\Psi = \frac{3c_ak_BT}{2Nb^2}\text{tr}(\boldsymbol{\mu} - \boldsymbol{\mu}_0) + \pi[\det(\boldsymbol{F}) - 1] \tag{3}$$

In the stress-free state, the chains' distribution of the end-to-end distance is usually assumed to be Gaussian, so the distribution tensor $\boldsymbol{\mu}_0$ assumes the simple diagonal form: $\boldsymbol{\mu}_0 = \frac{Nb^2}{3}1$ (Vernerey et al., 2017). Once the elastic potential energy is known, the stress state in the material can be obtained by recalling that the power per unit volume of the material is expressed by:

(a) r_z stretch (b) r_z

r_y r_y

r_x $\varphi_0(\boldsymbol{r})$ r_x $\varphi(\boldsymbol{r})$
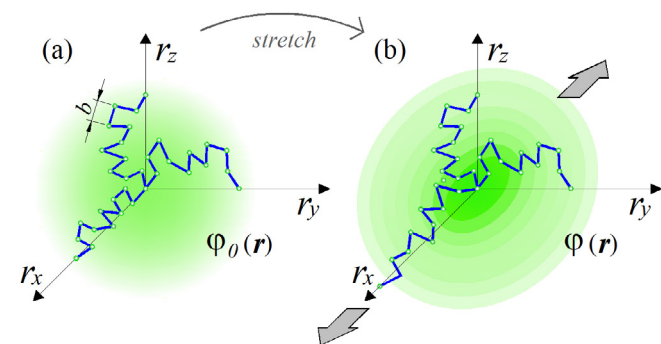
Fig. 1. Scheme of the end-to-end vector distribution field in a material point of the polymer in the stress-free state (a) and its counterpart in a stretched state corresponding to an elongation along the x direction (b). The color map intensity is proportional to the value of the distribution function $\varphi(\boldsymbol{r})$.

$$\frac{\partial\Delta\Psi}{\partial t} = \Delta\dot{\Psi} = \boldsymbol{\sigma} : \boldsymbol{D} \tag{4}$$

where $\boldsymbol{\sigma}$ is the Cauchy stress and $\boldsymbol{D}$ is the symmetric part of the velocity gradient tensor $\boldsymbol{L}$, $\boldsymbol{D} = \text{sym}\,\boldsymbol{L} = (\boldsymbol{L} + \boldsymbol{L}^T)/2$, being $\boldsymbol{L} = \dot{\boldsymbol{F}}\boldsymbol{F}^{-1}$.

In (4), the time rate of the energy $\Delta\Psi$ is required. For an isothermal process ($\dot{T} = 0$), it is given by (Vernerey et al., 2017):

$$\Delta\dot{\Psi} = \frac{3c_ak_BT}{2Nb^2}\langle(\dot{\varphi} - \dot{\varphi}_0)|\boldsymbol{r}|^2\rangle + \pi\text{tr}(\boldsymbol{L}) = \frac{3c_ak_BT}{Nb^2}(\boldsymbol{\mu} - \boldsymbol{\mu}_0)$$
$$: \boldsymbol{L} + \pi\text{tr}(\boldsymbol{L}) \tag{5}$$

in which, due to material incompressibility, $\text{tr}(\boldsymbol{L})=1 : \boldsymbol{L} = 0$, while the time derivative of the distribution function is provided by Eq. (7) below (Vernerey et al., 2017). From (4) and (5) the Cauchy stress tensor can be finally explicitly written:

$$\boldsymbol{\sigma} = J^{-1}\boldsymbol{P}\boldsymbol{F}^T = \frac{3c_ak_BT}{Nb^2}(\boldsymbol{\mu} - \boldsymbol{\mu}_0) + \pi 1 \tag{6}$$

The last expression of the time rate of the energy $\Delta\Psi$ in (5) has been obtained by applying the integration by parts on the term $\langle(\dot{\varphi} - \dot{\varphi}_0)|\boldsymbol{r}|^2\rangle$ after expressing the time derivative of the chains' end-to-end distance probability distribution functions φ, as shown in Eq. (7) below and by recalling the definition of the distribution tensor $\boldsymbol{\mu}$ (Vernerey et al., 2017). It is worth mentioning that the time derivative $\dot{\varphi}_0$ of the initial probability distribution function φ_0 is generally non-zero since it quantifies the change of φ_0 per unit time due to an applied deformation rate quantified by the tensor $\boldsymbol{L}$. By harnessing the conservation of the chain density during the deformation process (because of the absence of any damage or self-healing mechanisms), the time evolution of the distribution function $\dot{\varphi}$ in (5) can be determined from the relation $\frac{D}{Dt}\int_V \varphi(\boldsymbol{r},t)dV = 0$, which states the invariance in time of the chain concentration c_a, i.e. the number of chains in the volume V must be constant in time. By leveraging Reynolds' transport theorem, the material time derivative of the function φ for an incompressible medium becomes (Vernerey et al., 2017):

$$\dot{\varphi} = \frac{\partial\varphi(\boldsymbol{r},t)}{\partial t} = -\nabla\varphi \cdot \dot{\boldsymbol{r}} - \varphi(\nabla \cdot \dot{\boldsymbol{r}}) = -(\nabla\varphi \otimes \boldsymbol{r} + \varphi 1) : \boldsymbol{L}$$
$$= -(\nabla\varphi \otimes \boldsymbol{r}) : \boldsymbol{L} \tag{7}$$

Since the chain distribution space is embedded within a single point of the material and we are assuming an affine deformation, both the deformation gradient $\boldsymbol{F}$ and velocity gradient $\boldsymbol{L}$ can be considered to be homogeneous throughout the chain configuration space; thus, in Eq. (7) the rate of chains' deformation expressed as $\dot{\boldsymbol{r}} = \boldsymbol{L}\boldsymbol{r}$ has been used, where $\dot{\boldsymbol{r}}$ can be viewed as the velocity of a point $\boldsymbol{r}$ in the chain distribution space.

It is worth mentioning that, according to the freely-jointed chain model (FJC) adopted here, the mechanical response of the polymer is characterized by only the shear modulus G and the incompressibility constraint, while the quantities N and b of the chain do not play a role. The dependence on the last-mentioned parameters arise, for instance, when the chain energy is written by adopting the Langevin statistics (Doi, 1996). According to this assumption, the chain stretch is limited to be $\lambda \leq \lambda_{\max} = \sqrt{N}$; this entails that when the chain elongation tends to its contour length, i.e. $|\boldsymbol{r}| \rightarrow r_{max} \cong Nb$, the corresponding chain force tends to infinity, as the chain is assumed to be made of N rigid segments of equal length b.

2.2. Application of chain configuration statistics to LCEs

The first models to describe the behavior of liquid crystals (in the nematic, smectic and cholesteric phases) were mainly molecu-

lar force interaction-based and were aimed at obtaining the energy density of the material (Oseen, 1933; Frank, 1958). Continuum models that are based on the conservation of mass, linear and angular momentum, and energy laws were developed in subsequent works (Ericksen, 1961; Leslie, 1968, 1992; Ennis et al., 2006). Approaches based on the elastic and nematic deformation of LCEs (Jin et al., 2010; Biggins et al., 2009, 2012) and models that specifically describe the mechanical behavior of structural elements made of LCEs (such as plates, membranes, etc.) have been also developed (DeSimone, 2010; Agostiniani and DeSimone, 2017; Mihai and Goriely, 2020; Kowalski et al., 2018; Cirak et al., 2014). These modeling approaches have been applied to functional designs of LCE elements, which include materials that respond to external stimuli and undergo shape morphing (Ambulo et al., 2017; Jin et al., 2011; Fu et al., 2018).

The main physics-based theory of LCEs relies on the fundamental development of Warner, Terentjev et al. who extended the classical molecular rubber elasticity to nematic elastomers by accounting for the molecular shape anisotropy induced by the liquid crystalline order, i.e. by the nematic coupling to networks (Warner et al., 1988; Bladon et al., 1993, 1994). Nematic elastomers are characterized by the field of the director rotations – constituting an internal degree of freedom field – enabling the material to show spontaneous distortions, instabilities, and deformations. All of them take place at low energy cost. In nematic elastomers, the nematic preferential direction can be hindered in its rotation and this mechanism interacts with standard elasticity of the network (Bladon et al., 1993, 1994).

Within this context, our approach is similar to the classical molecular rubber elasticity-based model of LCEs (Warner and Terentjev, 2007; Warner et al., 1988; Bladon et al., 1993, 1994). It is based on the statistical description of the network arrangement through the use of the distribution tensor whose definition and meaning have been illustrated in Secttion 2.1 for a standard polymer. It accounts for a preferential chain orientation that is driven by the nematic mesogens. The model has a general applicability without any restriction to particular structural elements, is easily adaptable to elastomers characterized by multiple networks, allows to simply account for strain-rate effects and damage mechanics, and is readily implementable in a computational framework. As a matter of fact, when chain failure – responsible for the material micro damage – has to be accounted for, we must have $\dot{c}_a(t) = \langle \dot{\rho}(t) \rangle \leq 0$. Therefore, if a proper chain failure criterion is available (for instance based on the chain force exceeding a maximum bond force f_b, i.e. $|\boldsymbol{f}| = |\partial \psi(\boldsymbol{r})/\partial \boldsymbol{r}| \geq f_b$), the probability distribution function $\varphi(t, \boldsymbol{r})$ can be updated accordingly. In such a case, it happens to be $\langle \varphi(t, \boldsymbol{r}) \rangle \leq \langle \varphi_0(\boldsymbol{r}) \rangle = 1$.

We now describe how the statistical model discussed in Section 2.1 is suitable for modeling elastomers that have an orientational arrangement. The polymer chains in these cases have a preferential orientation due to the constraint provided by LC rods, which can be described quantitatively by the nematic order (also called the order parameter) (Warner and Terentjev, 2007).

Ordinary polymers in their stress-free state are usually characterized by a uniform distribution of their chains' orientations in 3D space; this implies that the distribution function is spherical (i.e. isotropic, with the corresponding distribution tensor $\boldsymbol{\mu}_0$ characterized by three identical eigenvalues, $\mu_{01} = \mu_{02} = \mu_{03}$). This distribution changes upon deformation by following the evolution law expressed by (9). Meanwhile, the chain backbones of nematic polymers are distorted according to the nematic ordering of the mesogens even in their stress-free state. This property can be described by introducing a proper non-isotropic distribution function φ_{0n}.

In light of this discussion, the statistical theory described previously for standard polymers also applies to elastomers that are characterized by a nematic order if the standard isotropic chain distribution function in the stress-free state is replaced by the following anisotropic distribution function φ_{0n} (Warner and Terentjev, 2007):

$$\varphi_{0n}(\boldsymbol{r}) = \left(\frac{3}{2\pi Nb}\right)^{\frac{3}{2}} \left(\frac{1}{\det \ell_0}\right)^{\frac{1}{2}} \exp\left[-\frac{3\boldsymbol{r} \cdot \ell_0^{-1} \boldsymbol{r}}{2Nb}\right] \tag{8}$$

where $\ell_0 = \ell_{0\perp} \mathbf{1} + (\ell_{0\parallel} - \ell_{0\perp}) \boldsymbol{n} \otimes \boldsymbol{n}$ is the so-called step-length tensor of the chain distribution, expressing the anisotropy of the polymer chains at the time instant just after the initial cross-linking. $\ell_{0\perp}$ and $\ell_{0\parallel}$ are the effective initial step lengths, measured parallel and perpendicular to the director $\boldsymbol{n}$, of a freely jointed chain, respectively (Warner and Terentjev, 2007; Warner et al., 1988). Here, $\ell_{0\parallel} \gg \ell_{0\perp}$ in a highly ordered chain network. When the network is in the isotropic state, the averaged square of the end-to-end distance is given by $\langle r_i^2 \rangle = \frac{Nb^2}{3}, i = 1, 2, 3$ (Doi, 1996), and the step length tensor reduces to $\ell_0 = b\mathbf{1}$. According to the definition of the distribution tensor given in Section 2.1, we introduce here the distribution tensor related to the statistical chain distribution provided by Eq. (8), $\boldsymbol{\mu}_n(\boldsymbol{r}, t = 0) = \boldsymbol{\mu}_{0n}(\boldsymbol{r}) = \langle \varphi_{0n}(\boldsymbol{r}) \boldsymbol{r} \otimes \boldsymbol{r} \rangle$. At the time of cross-linking, assumed to coincide with the initial stress-free state, the chains' end-to-end distancee distribution is provided by the function ρ_{0n} (or equivalently by its normalized counterpart φ_{0n}) and we have $\boldsymbol{\mu}_{0n} = \frac{Nb}{3} \ell_0$, being Nb the contour length of a polymer chain. Moreover, $\text{tr} \boldsymbol{\mu}_{0n} = 3 \frac{Nb^2}{3}$, irrespectively of the value of the nematic order parameter (see Eq. (10)).

In generic non-isotropic network chains, the distribution tensor $\boldsymbol{\mu}_{0n}$, corresponding to the distribution function φ_{0n} has three different eigenvalues ($\mu_{01}, \mu_{02}, \mu_{03}$), so it can be expressed in its principal directions' frame of reference as:

$$\boldsymbol{\mu}_{0np} = \boldsymbol{R}^T \boldsymbol{\mu}_{0n} \boldsymbol{R} = \sum_{i=1}^{3} \mu_{0i} \boldsymbol{m}_i \otimes \boldsymbol{m}_i \tag{9}$$

where $\boldsymbol{R}$ represents a proper second order rotation tensor and $\boldsymbol{m}_i$ is the versor of the $i - th$ principal direction at $t = 0$. When the principal directions of $\boldsymbol{\mu}_{0n}$ coincide with the axes of the coordinate frame of reference, it can be expressed simply as $\boldsymbol{\mu}_{0np} = \mu_{0i} \delta_{ij}, i, j = 1, 2, 3$.

A simple interpretation of these eigenvalues can be introduced by considering the standard deviation of the end-to-end distance component, $\langle r_{0i}^2 \rangle$, evaluated in the i-th principal direction: $\mu_{0i} = \langle r_{0i}^2 \rangle, i = 1, 2, 3$. In other words, these eigenvalues provide the standard deviation of the end-to-end distance in the three principal directions of $\boldsymbol{\mu}_{0n}$. In this case, the distribution tensor can be represented geometrically by an ellipsoid with semi-axes μ_{0i}, $i = 1, 2, 3$, oriented along the principal directions of $\boldsymbol{\mu}_{0n}$. This illustration allows us to visualize the distribution of the chains' end-to-end vectors in the spatial domain of the polymer, whose preferential orientation is henceforth considered to be caused by both the deformation and by temperature-dependent nematic preferential orientation of the liquid crystal rods.

In absence of any deformation, at a generic time instant t of the temperature evolution problem, the chain distribution tensor of the nematic polymer written in its principal directions frame of reference (here assumed to be aligned with that of the Cartesian coordinate frame of reference) can be related to the order parameter of the nematic phase of the liquid crystal polymer at the temperature $T(t)$ as frame of reference (the subscript p is omitted in $\boldsymbol{\mu}_n(t)$ for sake of simplicity) (Warner and Terentjev, 2007):

$$\boldsymbol{\mu}_n(t) = \frac{Nb}{3} \ell(t) = \frac{Nb}{3} b \begin{bmatrix} 1 - Q(t) & 0 & 0 \\ 0 & 1 - Q(t) & 0 \\ 0 & 0 & 1 + 2Q(t) \end{bmatrix} \tag{10}$$

where $Q(t) = \langle \frac{3}{2}\cos^2\theta(t) - \frac{1}{2}\rangle$ is the order parameter at the time t, and the mesogen units have been assumed, by way of example, to be preferentially aligned with the 3rd direction (z−axis) of the Cartesian coordinate frame of reference. In this expression, $\theta(t) = \theta(T(t))$ is the temperature-dependent angle formed by the mesogen axes and their average direction $\boldsymbol{n}$ of alignment at the time t. By observing Eq. (10) and considering the diagonal form of $\boldsymbol{\mu}_{np}$ when its principal directions are superposed to the coordinate axes, it can be recognized that $\mu_1 = \langle r_1^2(t)\rangle = \mu_2 = \langle r_2^2(t)\rangle \propto 1 - Q(t)$ and $\mu_3 = \langle r_3^2(t)\rangle \propto 1 + 2Q(t)$. In general, it happens to be that $\boldsymbol{\mu}_n(t) = \frac{Nb}{3}\boldsymbol{\ell}(t) = \frac{Nb}{3}b[(1 - Q(t))\boldsymbol{1} + 3Q(t)\boldsymbol{n}\otimes\boldsymbol{n}]$.

The parameter $Q(t)$ quantifies the degree of alignment of the molecular axes of the rods that constitute the liquid crystal phase of the elastomer. A nematic LCE shows a transversally isotropic mechanical behavior. In writing (10), we assume that the isotropic plane is the x, y plane, while the LC mesogens are aligned in the z-direction. Let's consider Eq. (10) at the time of cross-linking, i.e. at $t = 0$; the value $Q = 1$ indicates a nematic order where all the rods are perfectly aligned along the z direction, while the value $Q = 0$ refers to randomly oriented rods, such as in a perfectly isotropic arrangement of polymeric chains that has no nematic character. When $0 < Q < 1$, the rods display an intermediate degree of alignment along the z axis, and the intensity of the dispersion increases as $Q \to 0$. When $Q = -\frac{1}{2}$, all the LC rods belong to the x, y plane. From (10), it can be shown that the nematic order tensor $\boldsymbol{Q}_0$ (also called the de Gennes order tensor (De Gennes and Prost, 1993; Warner and Terentjev, 2007) represents the deviatoric part of the normalized tensor $\boldsymbol{\mu}_{0n}$. It is defined as follows:

$$\boldsymbol{Q}_0 = \frac{Q}{2}(3\boldsymbol{n}\otimes\boldsymbol{n} - 1) = \frac{1}{2}\left(3\frac{\boldsymbol{\mu}_{0n}}{Nb^2} - \boldsymbol{1}\right) \tag{11}$$

or equivalently, by using the step length tensor, $\boldsymbol{Q}_0 = \frac{1}{2}\left(\frac{\boldsymbol{\ell}_0}{b} - \boldsymbol{1}\right)$ (Jin et al., 2010).

It is worth recalling that, when the material undergoes a mechanical stretch, the distribution tensor $\boldsymbol{\mu}(t)$ changes accordingly. At a generic time t, it contains information on the average chain stretch in different directions. By considering Eq. (7), its time rate can be expressed as (Vernerey et al., 2017):

$$\dot{\boldsymbol{\mu}}_L(t) = \langle\dot{\varphi}(t)\boldsymbol{r}\otimes\boldsymbol{r}\rangle = \langle[-(\nabla\varphi(t)\otimes\boldsymbol{r}):\boldsymbol{L}(t)]\boldsymbol{r}\otimes\boldsymbol{r}\rangle \tag{12$_1$}$$

$$= \langle\varphi(t)\boldsymbol{r}\otimes\boldsymbol{r}\rangle\boldsymbol{L}(t) = \boldsymbol{L}(t)\boldsymbol{\mu}(t) + [\boldsymbol{L}(t)\boldsymbol{\mu}(t)]^T \tag{12$_2$}$$

where the subscript $\dot{\mu}_L$ has been used to indicate that the time variation is affected by the deformation only. In order to get the final result, the integration by parts on the first term in Eq. (12$_1$) has been used, further $\nabla\boldsymbol{r} = 1$ and the boundary terms have been neglected since they decay to zero at the boundary of the chain configuration space, i.e. $\varphi(|\boldsymbol{r}| \to \infty) = 0$.

2.3 Energy of a nematic elastomer

At a generic time t, the free energy (having an entropic nature) per unit volume of the material, is obtained by adding up the free energy of the chains contained in such a volume, averaged over the chain conformation space, i.e. (Warner and Terentjev, 2007; Warner et al., 1988):

$$\Psi = -c_a k_B T\langle\ln\varphi_n\rangle = \frac{3c_a k_B T}{2Nb}\text{tr}(\boldsymbol{\ell}^{-1}\langle\boldsymbol{r}\otimes\boldsymbol{r}\rangle) + C \tag{13}$$

where the distribution function in the current state, given by Eq. (8), has been used, while C is an additive constant that can be neglected. By using the affine deformation hypothesis, the current end-to-end vector is simply expressed through the deformation gradient tensor

as $\boldsymbol{r} = \boldsymbol{F}\boldsymbol{r}_0$, so the free energy density is expressed by using the indicial notation as follows (Bladon et al., 1994):

$$\Psi = \frac{3G}{2Nb}\text{tr}(\ell_{lk}^{-1}\langle F_{kj}r_{0j}F_{li}r_{0i}\rangle) + \cdots = \frac{G}{2}\text{tr}(\ell_{0ij}F_{kj}\ell_{kl}^{-1}F_{li}) + \cdots \tag{14}$$

having used the result $\langle r_{0i}r_{0j}\rangle = \frac{Nb}{3}\ell_{0ij}$ (in the isotropic state it is $\langle r_{0i}r_{0j}\rangle = \frac{Nb^2}{3}\delta_{ij}$) (Warner and Terentjev, 2007); it represents an extension of the free energy provided by the classical rubber elasticity theory (Doi, 1996). The energy density variation, expressed by using Eq. (14), evaluated with respect to the initial stress-free state for which we have $\Psi_0 = 3G/2$ becomes:

$$\Delta\Psi(t) = \frac{G}{2}\left[\text{tr}\left(\boldsymbol{F}\boldsymbol{\ell}_0\boldsymbol{F}^T\boldsymbol{\ell}^{-1}\right) - 3\right] \tag{15}$$

Now, by assuming that the polymer initially has a chain arrangement described by the distribution tensor $\boldsymbol{\mu}_{0np}$ provided by Eq. (10) at $t = 0$, i.e. $\boldsymbol{\mu}_{0np} = \boldsymbol{\mu}_{np}(t = 0)$, the energy per unit volume of the polymer given by Eq. (3) can be rewritten by considering that $\text{tr}\boldsymbol{\mu}_{0np} = \frac{Nb}{3}\text{tr}\boldsymbol{\ell}_0 = 3\frac{Nb^2}{3}$ (see Eq. (10) in Secttion 2.2). The following expression is obtained:

$$\Delta\Psi(t) = \Psi(t) - \Psi_0 = \frac{3G}{2Nb^2}\text{tr}(\boldsymbol{\mu}_n(t) - \boldsymbol{\mu}_{0n})$$
$$= \frac{G}{2}\left(\text{tr}\frac{3\boldsymbol{\mu}_n(t)}{Nb^2} - 3\right) \tag{16}$$

By considering how the order tensor transforms between the reference and spatial domain, $\boldsymbol{Q} = J^{-1}\boldsymbol{F}\boldsymbol{Q}_0\boldsymbol{F}^T$ (Warner and Terentjev, 2007), and using Eq. (11), the relation between the distribution tensor in the current deformed configuration and the initial step length tensor can be found to be:

$$\boldsymbol{\mu}_n = \frac{Nb}{3}\boldsymbol{F}\boldsymbol{\ell}_0\boldsymbol{F}^T \tag{17}$$

At the time of cross-linking, i.e. at $t = 0$ prior to deformation, the previous relation leads to $\boldsymbol{\mu}_n(t = 0) = \boldsymbol{\mu}_{0n} = \frac{Nb}{3}\boldsymbol{\ell}_0$ as already mentioned above.

It is also worth recalling the microscopic Maier-Saupe theory of the phase transition in nematic liquid crystals, which is applicable only to homogeneous phases and is based on a molecular field treatment of long-range contributions to the intermolecular potential (Maier and Saupe, 1958). It allows predicting the orientational properties of nematic elastomers whose molecules interact via an orientation-dependent potential. According to such a theory, a molecule interacts with an appropriately chosen external field whose role is to replace the interaction with all the other molecules. The probability distribution function for the orientation of a molecule in presence of the external field can be expressed through the Gibbs distribution, $\phi(\boldsymbol{r}) = \frac{1}{Z}\exp\left(-\frac{\psi(\boldsymbol{r})}{k_B T}\right)$, where Z is the *partition function* (or configuration integral) used in classical statistical mechanics. It is defined as $Z = \int_\Omega \exp\left(-\frac{\psi(\boldsymbol{q})}{k_B T}\right)d\boldsymbol{q}$ (where $\boldsymbol{q}$ is a set of parameters defining the state of the system and $\psi(\boldsymbol{q})$ is the conformational (free) energy), and describes the statistical properties of a system in a thermodynamic equilibrium (Gō and Scheraga, 1976; Lifson, 1964). By considering a chain network system, whose strands obey the FJC model in the Gaussian regime and the function $\psi(\boldsymbol{r})$ is that provided in Section. 2.1, the partition function becomes $Z = \left(\frac{2\pi Nb^2}{3}\right)^{3/2}$, and finally, we arrive at the standard distribution function shown in Section. 2.1, i.e. $\phi(|\boldsymbol{r}|) = \varphi_0(|\boldsymbol{r}|)$. From this perspective, the microscopic Maier-Saupe theory can be reduced to the statistical description of LCEs.

3. Mechanics of stimulus-responsive LCE

3.1. Extension of the statistical chain distribution to ordered chain arrangement

Elastomers become responsive to external stimuli by harnessing the active character of molecules or moieties embedded in their network backbone. Mechanophores are examples of molecules that undergo physical or chemical transformations in the presence of mechanical stresses (Silberstein et al., 2013; Brighenti et al., 2019). During activation, their polymer chains are reconfigured, and a reverse process returns these chains to their initial state.

A transition between the two states occurs when a sufficient amount of energy is imparted to the system, allowing the energy barrier that separates the two states to be overcome (Brighenti et al., 2019; Hänggi et al., 1990). Within this context, when LCEs are exposed to a sufficiently intense source of thermal energy or light, they lose their initial nematic order and assume a disordered isotropic mesogen arrangement. We denote as ΔG_{ni} the energy barrier that must be overcome for there to be a transition from a nematic state to an isotropic state (the forward process). The energy barrier for the reverse transition to occur is denoted as ΔG_{in} (the backward process). This isotropic to nematic phase transition occurs when the temperature is lowered below the LCE's material-dependent transition temperature T_{NI} (Fig. 2).

The function $s(T)$ in Fig. 2.b represents how the order parameter $Q(T)$ changes with temperature. It can be thought of as an activation function and lies within the interval $0 < s < 1$. At a temperature close to the threshold temperature T_{NI}, there is a transition from the fully nematic ($Q = 1$) to the fully isotropic ($Q = 0$) state. The sigmoid function (also called the logistic function) is a simple and suitable expression for this type of activation function $s(T)$. Here, it is expressed by $s(T) = Q(T) = \frac{Q_0}{1+\exp\frac{T-T_{NI}}{c}}$, where Q_0 is the initial value of the nematic order and c is a material-specific constant parameter, while T_{NI} is the nematic-isotropic transition temperature. The time derivative of the order parameter is given by $\dot{Q} = \frac{ds}{dT}\frac{dT}{dt} = -\frac{\exp\frac{T-T_{NI}}{c}}{Q_0 c}s^2\dot{T}$. The corresponding time derivative of the network distribution tensor is:

$$\dot{\boldsymbol{\mu}}_n = \frac{\partial \boldsymbol{\mu}_n}{\partial t} = 2\frac{Nb^2}{3}\left(\dot{Q} - \boldsymbol{W}Q + Q\boldsymbol{W}\right) \tag{18}$$

being $\boldsymbol{W} = 1/2(\nabla\dot{\boldsymbol{u}} - \nabla\dot{\boldsymbol{u}}^T)$ the spin tensor (Zhang et al., 2019).

This tensor is zero when the order parameter is constant in time, such as when the temperature is constant ($\dot{T} = 0$) or when the temperature is well below the T_{NI} temperature.

Since we now have the time derivatives related to the deformation and to the nematic-isotropic transition (we assume these derivatives are independent of each other), it is possible to determine the temporal evolution of the distribution tensor so that it is fully known at any time instant τ during the thermo-mechanical process:

$$\boldsymbol{\mu}(t) = \boldsymbol{\mu}_n(0) + \int_0^t [\dot{\boldsymbol{\mu}}_L(\tau) + \dot{\boldsymbol{\mu}}_n(\tau)]d\tau \tag{19}$$

being $\boldsymbol{\mu}(t = 0) = \boldsymbol{\mu}_n(t = 0) = \boldsymbol{\mu}_{0n}$ the initial distribution tensor of the material, while the total chain distribution tensor rate has been expressed as $\dot{\boldsymbol{\mu}}_L + \dot{\boldsymbol{\mu}}_n$, i.e. the evolution of the network chains is due to both the mechanical deformation and the nematic change induced, for instance, by a temperature variation of the material.

Now, the distribution tensor can be inserted into Eq. (6) to get the stress state in the material,

$$\sigma(t) = \frac{3c_a k_B T}{Nb^2}\left(\boldsymbol{\mu}(t) - \boldsymbol{\mu}_{0n}\right) + \pi(t)\mathbf{1} \tag{20}$$

Here, the hydrostatic pressure $\pi(t)$ can be determined from the boundary conditions of the problem.

3.2 Computational aspects

The problem formulated above can be conveniently rewritten in its variational form through the stationary condition of the potential energy Π. We consider a region of material occupying the domain $\mathscr{B}_0$ bounded by $\partial\mathscr{B}_0$. The first variation of Π in the reference configuration has the following form:

$$\delta\Pi = \int_{\mathscr{B}_0} \delta\Psi dV + \delta\Psi_{ext}$$
$$= \int_{\mathscr{B}_0} \delta\Psi_e(\boldsymbol{F})dV - \int_{\mathscr{B}_0} \boldsymbol{B} \cdot \delta\boldsymbol{u}dV - \int_{\partial\mathscr{B}_0} \boldsymbol{t} \cdot \delta\boldsymbol{u}dA = 0, \tag{21}$$

where Ψ_{ext} is the energy of the external mechanical loads $\boldsymbol{B}$ and $\boldsymbol{t}$, which correspond to the prescribed body forces and the surface tractions, respectively. The variation of the functional (21) with respect to the displacement field $\boldsymbol{u}$ yields:

$$\delta_{\boldsymbol{u}}\Pi = \int_{\mathscr{B}_0} \frac{\partial\Psi}{\partial\nabla\boldsymbol{u}}\delta\nabla\boldsymbol{u}dV - \int_{\mathscr{B}_0} \boldsymbol{B} \cdot \delta\boldsymbol{u}dV - \int_{\partial\mathscr{B}_0} \boldsymbol{t} \cdot \delta\boldsymbol{u}dA$$
$$= \int_{\mathscr{B}_0} [\nabla \cdot \boldsymbol{P} - \boldsymbol{B}]\delta\boldsymbol{u}dV + \int_{\partial\mathscr{B}_0} [\boldsymbol{P} \cdot \boldsymbol{N} - \boldsymbol{t}] \cdot \delta\boldsymbol{u}dA = 0 \tag{22}$$

The variational statement can be discretized by introducing a proper discretization of the displacement field and of its gradient, i.e.:

$$\boldsymbol{u}_p = \sum_{i=1}^{n_n} [N]_i\tilde{\boldsymbol{u}}_i, \nabla \cdot \boldsymbol{u}_p = \nabla_{\boldsymbol{X}} \sum_{i=1}^{n_n} [N]_i\tilde{\boldsymbol{u}}_i = \sum_{i=1}^{n_n} [B]_i\tilde{\boldsymbol{u}}_i \tag{23}$$
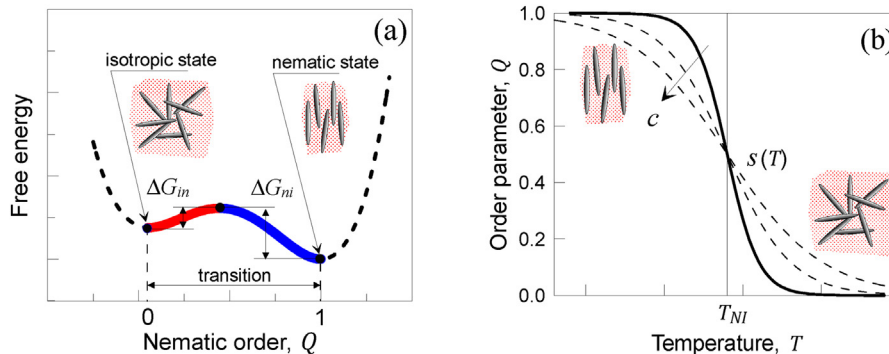
Fig. 2. Schematic of the energy vs nematic order for a LCE (a). Transition from the ordered state ($Q = \mathbf{1}$) to the isotropic one ($Q = 0$) when increasing the temperature above the T_{NI} (b). The two states, namely the nematic and the isotropic correspond to two potential wells of the free energy function.

The subscript p refers to interpolated quantities that are obtained by using the corresponding nodal values indicated with $\tilde{\boldsymbol{u}}_i$. In the discretization above, n_n is the number of nodes, and $[N]_i$ and $[B]_i$ denote the standard shape function and the compatibility matrix associated with the $i - th$ node, respectively. The discretized form of the energy stationarity is a force balance condition. For a single finite element having volume V_0^e and outer surface A_0^e, we have:

$$\{R\}_{\boldsymbol{u}}^e = \{R\}_{\boldsymbol{u}}^{e,int} - \{R\}_{\boldsymbol{u}}^{e,ext}$$
$$= \int_{V_0^e} [B]^T \boldsymbol{P} dV - \int_{V_0^e} [N]^T \boldsymbol{B} dV + \int_{A_0^e} [N]^T \boldsymbol{t} dA = \{0\} \qquad (24)$$

This provides the condition of a vanishing residual force vector $\{R\}_{\boldsymbol{u}}^e$, defined as the difference between the nodal forces (corresponding to the internal stress state, $\{R\}_{\boldsymbol{u}}^{e,int}$), and the corresponding nodal values of the external actions, $\{R\}_{\boldsymbol{u}}^{e,ext}$. Upon linearization of (24), the above-stated residual force vector must be made to vanish by considering the whole problem domain discretized by ne finite elements. The solution is obtained by iteratively solving the following system of equations:

$$[K]_T \Delta u = -R_u, \quad \text{with} \quad [K]_T = \mathbb{A}_{e=1}^{ne} [K]_T^e, \qquad (25)$$

where $\boldsymbol{K}_T^e = \frac{\partial \boldsymbol{R}_{\boldsymbol{u}}^e}{\partial \boldsymbol{u}} = \int_{V_0^e} [B]^T \frac{\partial^2 \Psi}{\partial \boldsymbol{E}^2} [B] dV$ is the standard tangent stiffness matrix, $\boldsymbol{E}$ is the Green-Lagrange deformation tensor, and $\mathbb{A}$ indicates the assembly operator.

For the sake of clarity, a brief description of the main steps of the computational multi-scale analyses is reported hereafter. Initially, the material is assumed to be in the stress-free state and the displacement field is zero everywhere. As the time goes by, the temperature distribution is evaluated at the Gauss points of the discretized domain by solving the standard Fourier heat conduction problem. The temperature increase is thus related to the change of the nematic order of the material and therefore both the distribution function φ_n as well as the distribution tensor $\boldsymbol{\mu}_n$ evolve, providing all the information required to evaluate the stress state of the material (see Eq. (20)).

By using the above described theoretical framework applied at the finite element's Gauss point level, the internal stress state of the material, governed – in absence of any applied mechanical deformation – only by the nematic-isotropic transition, leads to a vector of element's nodal forces corresponding to such a stress state, $\{R\}_{\boldsymbol{u}}^{e,int}$. Such a nodal force vector, together with the external forces nodal vector $\{R\}_{\boldsymbol{u}}^{e,ext}$, provides the element's unbalanced residual force vector $\{R\}_{\boldsymbol{u}}^e$ (24), whose norm must be brought throughout the iterative solution procedure to a value smaller than a suitably small tolerance. The incremental nodal displacement correction vector $\Delta \boldsymbol{u}$ is determined at each iteration and used to update the current nodal displacements vector of the discretized problem. The staggered scheme for the solution of the thermal and the mechanical problems can be conveniently adopted to solve the coupled problem, provided that the time step is sufficiently small, can be conveniently adopted to solve the coupled problem. Both the problems are solved by accounting for the large displacements taking place in the material. It is worth noticing that the numerical assessment of the distribution tensor through the computation of the integral $\langle \varphi_n \boldsymbol{r} \otimes \boldsymbol{r} \rangle$ over the 3D chain configuration space requires a big computation effort. In fact, for each finite element the computational cost is proportional to $M^3 \cdot N_{GP}$ where, at a single Gauss point $M = M_x = M_y = M_z$ is the number of quadrature points used for discretizing each direction of the 3D chain space, and N_{GP} is the total number of Gauss points within the finite element.

Thus, in order to calculate the current distribution tensor $\boldsymbol{\mu}_n(t)$ starting from its initial counterpart (assumed to be known), $\boldsymbol{\mu}_{0n} = \boldsymbol{\mu}_n(0)$, it is more convenient to use Eq. (19); this approach requires evaluating the rates $\dot{\boldsymbol{\mu}}_L$ and $\dot{\boldsymbol{\mu}}_n$, as illustrated above.. In particular, if only the temperature change takes place in the material, the knowledge of $\dot{\boldsymbol{\mu}}_n$ suffices to evaluate $\boldsymbol{\mu}_n(t)$.

4. Experimental observations on 3D printed LCEs

Here, we briefly summarize the experimental results on 3D printed LCEs from Kotikian et al. (2019) which serve to both test and validate our model. In this prior study, reversible hinges were made by 3D printing LCE bilayers with orthogonal director alignment using high operating-temperature direct ink writing (HOT-DIW) connected to two rigid acrylate plates (see Fig. 4a). Each LCE layer exhibits a large contraction along the printing direction (parallel to the director alignment) and an expansion in orthogonal direction, the resulting strain mismatch across the bilayer induces a bending response when the hinge is heated above T_{NI}. We compare the predictions from our model to the experimentally observed response.

Two oligomeric LCE inks with pre-cross-linking transition temperatures (or "T_{NI}") of 24 °C and 94 °C (referred to as LT_{NI} and HT_{NI} inks, respectively) were synthesized. These values were obtained via differential scanning calorimetry (DSC) measurements, but after the inks were cross-linked during the 3D printing process, the transition between the fully nematic and fully isotropic states occurred over a range of temperatures: LT_{NI} specimens started bending near 25 °C and become fully isotropic at 92 °C, while the HT_{NI} specimens start bending near 60 °C and become fully isotropic at 127 °C. The difference in transition temperatures occurs due to disparities in ink design, namely backbone flexibility and cross-linking chemistry. Different bending angles are obtained upon heating by programming the length, width and chemistry of the LCE bilayers.

Data from standard tensile tests on LCE bilayers with perpendicularly oriented mesogens (Fig. 3a1), as well as on the acrylate material, are reported in Fig. 3b–d. These results are used to determine the main mechanical parameters needed for the statistical model discussed previously, such as the chain concentration per unit volume, which is related to the material's shear modulus.

To characterize the behavior of these LCE hinges, each specimen has been heated in an oil bath (see Fig. 4a) to switch the material from the transversally isotropic (i.e., nematic) state to the isotropic one. Bending angles were measured as a function of temperature, by imaging the folding process with a camera. The results for specimens that are 0.25 mm thick and have varying width are shown in Fig. 4. We refer the reader to Kotikian et al. (2019) for more details on specimen fabrication and characterization.

5. Numerical simulations and discussion

In order to test and validate our model, in this section we present some numerical simulation results and compare them with experimental measurements. In particular, we firstly investigate a simple case of a monodomain nematic elastomer sample, while in the second case we investigate the thermal variation-induced bending response of soft actuators constituted by a bilayer hinge of LCE, see Section 4.

5.1 Simulation of a temperature-driven monodomain LCE sample

The temperature change-induced deformation of a rectangular sample strip made of polysiloxane monodomain nematic elastomer (Clarke et al., 2001) is considered in this sub-section.
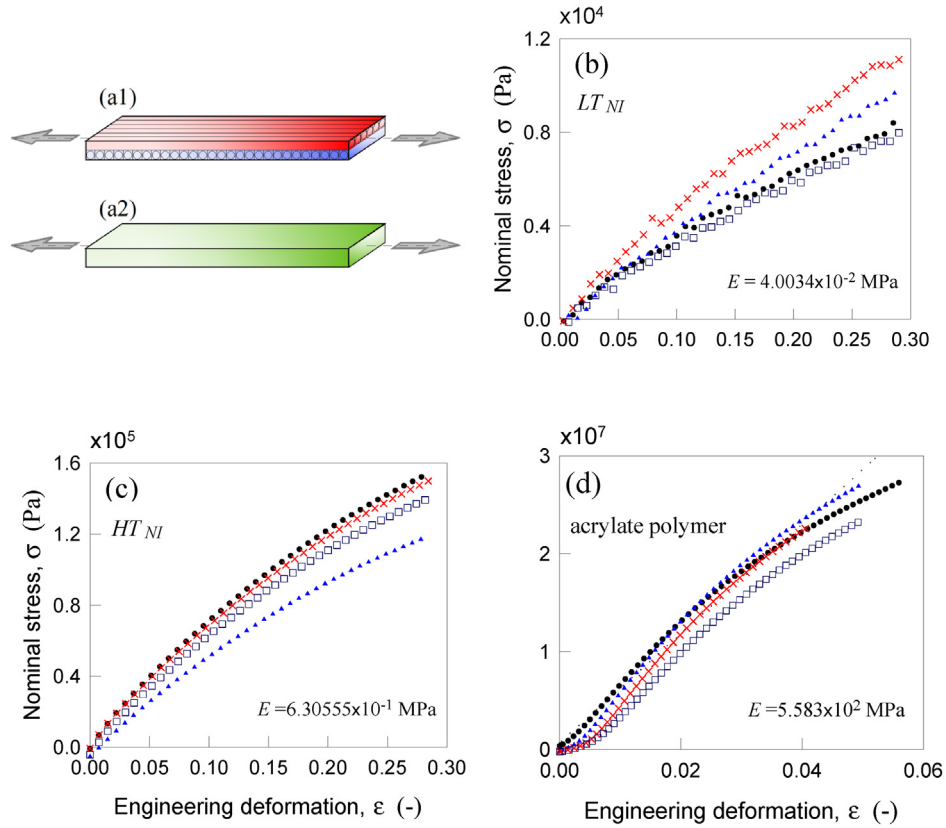
Fig. 3. Scheme of the specimen made of two acrylate plates joined with an LCE actuator (a1) and of the acrylate bar. Stress–strain testing results for a single layer made of low LT_{NI} LCE (b) and high HT_{NI} LCE (c). Stress–strain testing results for the acrylate polymer constituting the two bats of the LCE device (d). Adapted from Kotikian et al. (2019).
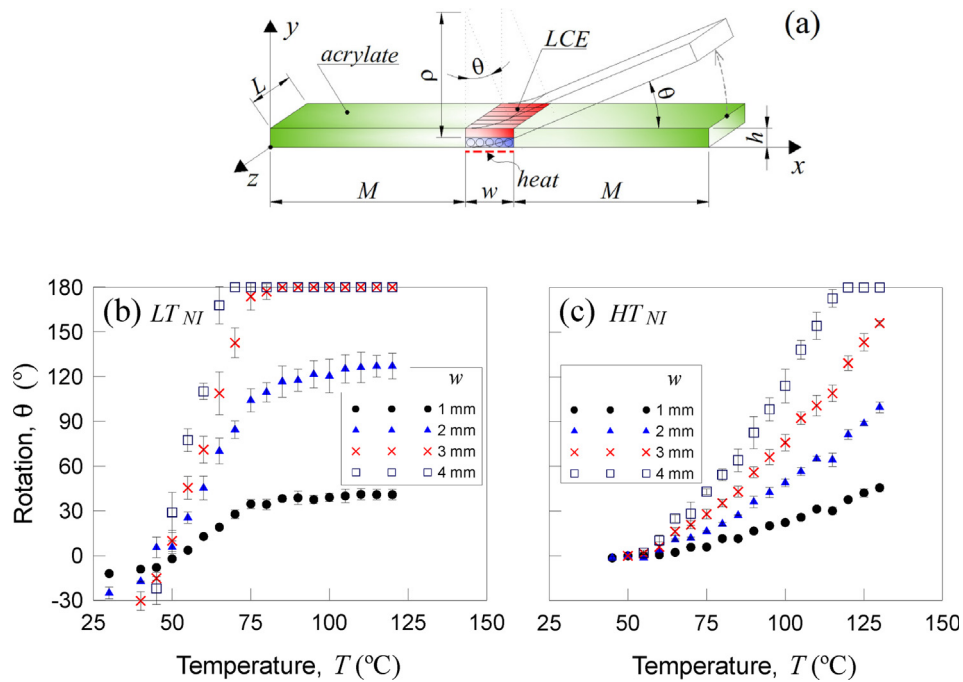
Fig. 4. Schematic of the bending experiments (a). Experimentally measured rotation vs temperature for the specimens with different sizes of the LCE hinge part. LCE with lowest actuation temperature LT_{NI} (b), and highest actuation temperature HT_{NI} (c). Adapted from Kotikian et al. (2019).

The LCE element has an initial length L_0, while the nematic director in the undeformed state is oriented parallel to the (vertical) y-axis (Fig. 5). We adopt here the $Q - T$ relationship reported in Section 3.1; in order to investigate the effects of the material-dependent parameter c, three different values for such a constant, namely $c = 6; 10; 16$, are adopted. In the experimental test the

specimen is cooled down to about 30 °C from an initial temperature of about 120 °C, making the specimen expand in the y-direction because of the isotropic-nematic transition ($\lambda_y \geq 1$). See dotted lines in Fig. 5a,b (Clarke et al., 2001). On the other hand, since the above-mentioned transition is fully reversible, we start our FE simulations from an initial nematic state at nearly room temperature $T = 30$ °C with $Q_0 = 0.46$ and heat up the LCE element above the nematic transition temperature $T_{NI} = 86$ °C (Clarke et al., 2001). This induces the isotropization of the material with a consequent contraction in the y-direction ($\lambda_y \leq 1$). The initial conditions of the experimental and of the numerical simulation are indicated by the blue and red square in Fig. 5b, respectively. In order for the results to be compared, for sake of comparison only the absolute value of the stretch difference between different states is meaningful.

Overall, the model results are in reasonable agreement with the experimental ones, both in term of the nematic order (Fig. 5a) and stretch evolution (Fig. 5b) with the temperature change. It can be appreciated that lower values of the parameter c (e.g. $c = 6$) lead to a sharp nematic-isotropic transition, while to greater values of c corresponds a more gradual one.

The deformed shapes of the LCE element are obtained from the numerical simulations at two different temperatures and by adopting the three above-mentioned values of c are reported in Fig. 5c, d; at $T = 60$ °C (points A_1, B_1 and C_1 in Fig. 5a) and at $T = 110$ °C (points A_2, B_2 and C_2 in Fig. 5a), respectively. Interestingly, the element with the lowest c is the least contracted at $T = 60$ °C $< T_{NI}$, since Q changes only slightly up to this temperature; when a higher temperature $T = 110$ °C $> T_{NI}$ is considered, the contraction is similar to those obtained by adopting the other values of c, so for a sufficiently high temperature above the T_{NI}, the deformation is almost independent of c which plays a role only during the transition.

5.2 Numerical simulation of a 3D printed LCE elastomer element

In this section, we describe numerical simulations of the thermally induced response of LCE elements discussed in Section 4. Two LT_{NI} hinges (one with $h = 0.25$ mm and $w = 1$ mm, the other with $h = 0.50$ mm and $w = 2$ mm) and two HT_{NI} hinges (one with $h = 0.25$ mm and $w = 1$ mm, the other with $h = 0.25$ mm and $w = 2$ mm) have been considered. Since we wish to capture a full transition from a nematic to an isotropic state, we conduct our simulations of LT_{NI} specimens assuming a transition temperature of $T_{NI} = 50$ °C. For the HT_{NI} LCE, we assume $T_{NI} = 95$ °C. As discussed in Section 4, both of these temperatures lie about halfway within the range of experimentally observed actuation and should not be confused with the T_{NI} values obtained via differential scanning calorimetry (DSC) for pre-cross-linked LCE inks (Kotikian et al., 2019). In our frame of reference (shown in Fig. 4a), the bottom halves of the LCE elements are printed such that the mesogens are aligned with the z-direction, while the upper halves are aligned with the x-direction. By fitting to experimental tests results, the coefficient c of the function $s(T)$ has been assumed to be equal to $c = 10$. The analyses are performed assuming a plane stress condition and fast heat transfer through the material because of the small size of the specimens (see Fig. 3a). Though heating in the angle measurement experiments were conducted in an oil bath (Kotikian et al., 2019), we assume heating via a hot plate in contact with the bottom face of the actuators in our simulations. Due to the fast rate of heat transfer, the bending angles should be very similar under either heating method. The temperature evolution within the material is determined by solving the heat conduction problem in the whole element, while adopting a thermal conductivity coefficient equal to $\kappa = 0.2$ W/mK and a specific heat of $C = 1050$ J/Kg K (Anderson, 1966; Choy, 1977; Wen, 2007). The thermal expansion of the material is assumed to be negligible within the temperature
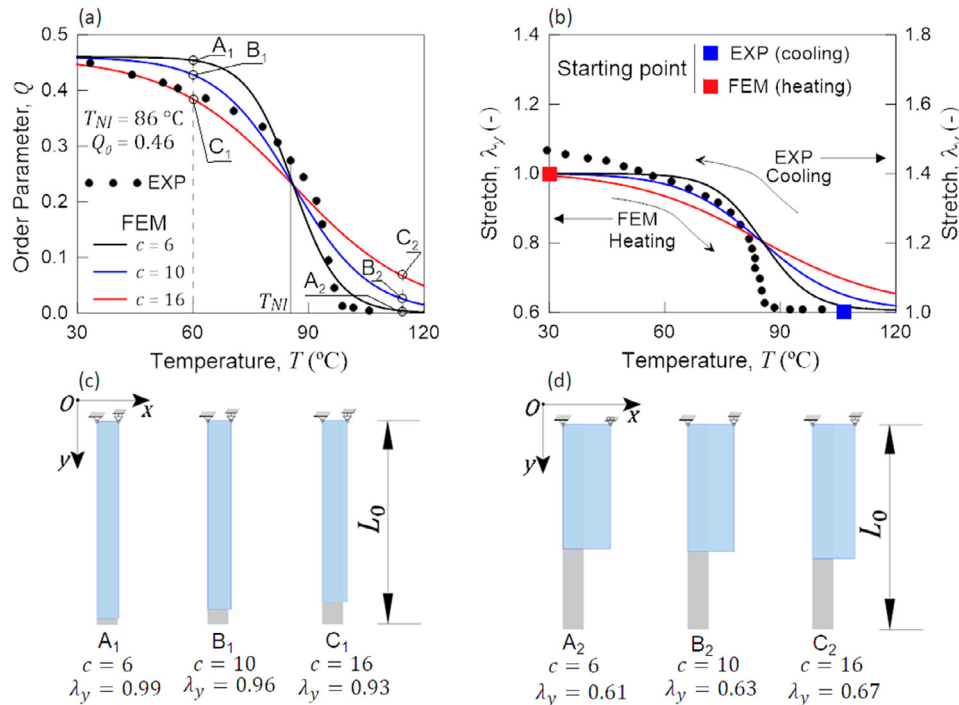
Fig. 5. Comparison between experimental measurements (Clarke et al., 2001) and simulations of the $Q - T$ dependence for different values of the material parameter c (a). Experimental and numerical $\lambda_y - T$ curves (b). Experimental stretches are reported with respect to the right-hand side vertical axis, while numerical ones are reported with respect to the left-hand side one. Comparison of the undeformed (grey) and deformed (light blue) shapes of the element provided by the model for different values of c, at $T = 60$ °C (A_1, B_1, C_1) (c) and at $T = 110$ °C (A_2, B_2, C_2) (d). (For interpretation of the references to color in this figure legend, the reader is referred to the web version of this article.)

range considered. It is worth mentioning that the values of the thermal conductivity and of the specific heat do influence the time evolution of the temperature field within the material. Meanwhile, the temperature distribution is nearly uniform and does not depend on such a coefficient at steady state.

It is worth mentioning that the problem of finding the 3D shape shown by nematic elastomer sheets undergoing spatially inhomogeneous deformations has been considered in several researches (Modes et al., 2011; Aharoni et al., 2014; Mostajeran, 2015; Plucinsky et al., 2016; Griniasty et al., 2019). As a matter of fact, the variation of the spatial orientation of the local director field can lead to a surface with a Gaussian curvature, i.e. a non-developable surface; in this perspective, when the application of nematic sheets as actuators is concerned, the inverse problem of
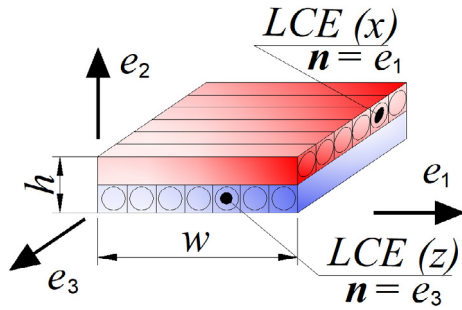
Fig. 6. Scheme of the nematic bilayer with the adopted reference frame of reference. e_1, e_2, e_3 are the unit vectors identifying of the coordinate axes x, y, z.

finding the director field required to get a desired deformed shape, represents a crucial task that has also been considered in the literature (Aharoni et al., 2014; Mostajeran, 2015; Griniasty et al., 2019).

In the following, we compare our statistical mechanics approach to a rigorous theoretical model that is suitable for describing the bending of nematic plates (Agostiniani and DeSimone, 2017). According to this approach, a region of the LCE that has nematic order defined by the director n (i.e. the unit vector representing the local order of the nematic mesogens) deforms spontaneously when an isotropic-to-nematic transition occurs. This deformation is quantified by the following right Cauchy-Green deformation tensor (Agostiniani and DeSimone, 2017):

$$C_h = F_h^T F_h = a_h^{2/3} n \otimes n + a_h^{-1/3} (1 - n \otimes n) \tag{26}$$

where a_h is a material-dependent parameter that varies with temperature and it is fitted from the experimental data. It can also be a function of the plate thickness h; however, in this study we assume a_h to be constant for each specimen. It is worth recalling that the rigorous theoretical approach proposed in (Agostiniani and DeSimone, 2017) has been derived for vanishingly small spontaneous shape change; however, the above-mentioned theoretical model has been here considered for sake of providing an approximate comparison – in term of the order of magnitude of the temperature-change-induced deformation and the corresponding bilayer rotation – with our numerical results based on the micromechanical model presented in the previous sections.

In Eq. (26) $n = e_3$ in the lower layer while $n = e_1$ in the upper one (Fig. 6). Once the right Cauchy-Green deformation tensor C_h
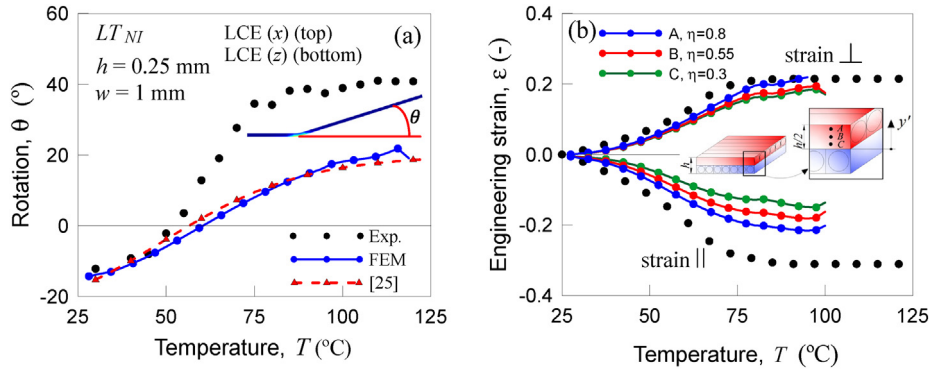

Fig. 7. Rotation angle vs temperature (measured at the bottom of the beam) for the LT_{NI} LCE hinge with thickness $h = 0.25$ mm and width $w = 1$ mm. Comparisons between the FE, experimental (Kotikian et al., 2019) theoretical data obtained from the theory in Agostiniani and DeSimone (2017) are reported (a). Engineering strain parallel and perpendicular to the nematic order director (b).
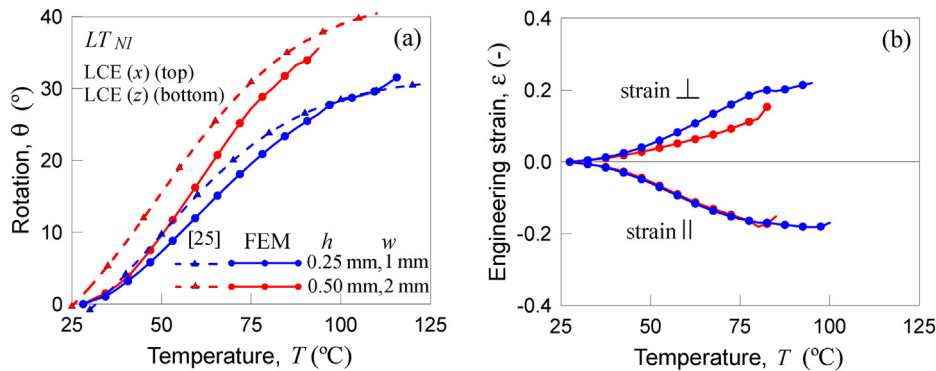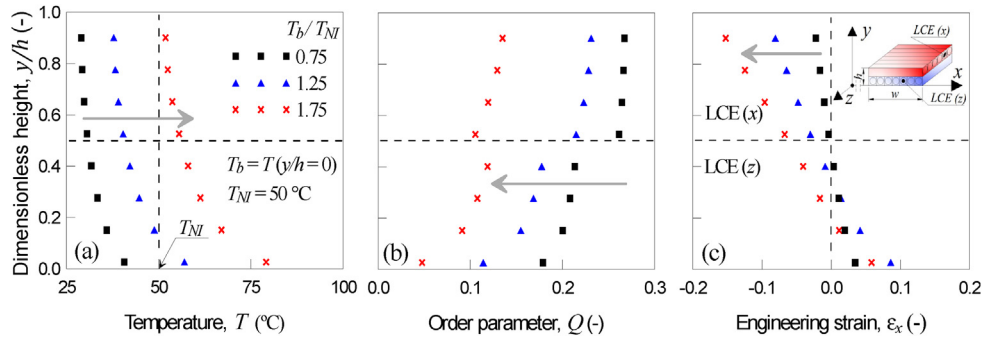

Fig. 8. Bending angle vs temperature for the LT_{NI} LCE hinge with thickness $h = 0.25, 0.50$ mm and width $w = 1, 2$, respectively. FE analysis results are compared with the theoretical model prediction (Agostiniani and DeSimone, 2017) (a). Engineering strain parallel and perpendicular to the nematic order director (b).

Fig. 9. Profiles of the temperature (a), of the order parameter Q (b) and of the longitudinal strain ε_x (c) along the LT_{NI} LCE hinge centerline vertical section ($h = 0.25$ mm, $w = 1$ mm) provided by the present model. Different values of the dimensionless temperature T_b/T_{NI} are considered, namely 0.75, 1.25 and 1.75.
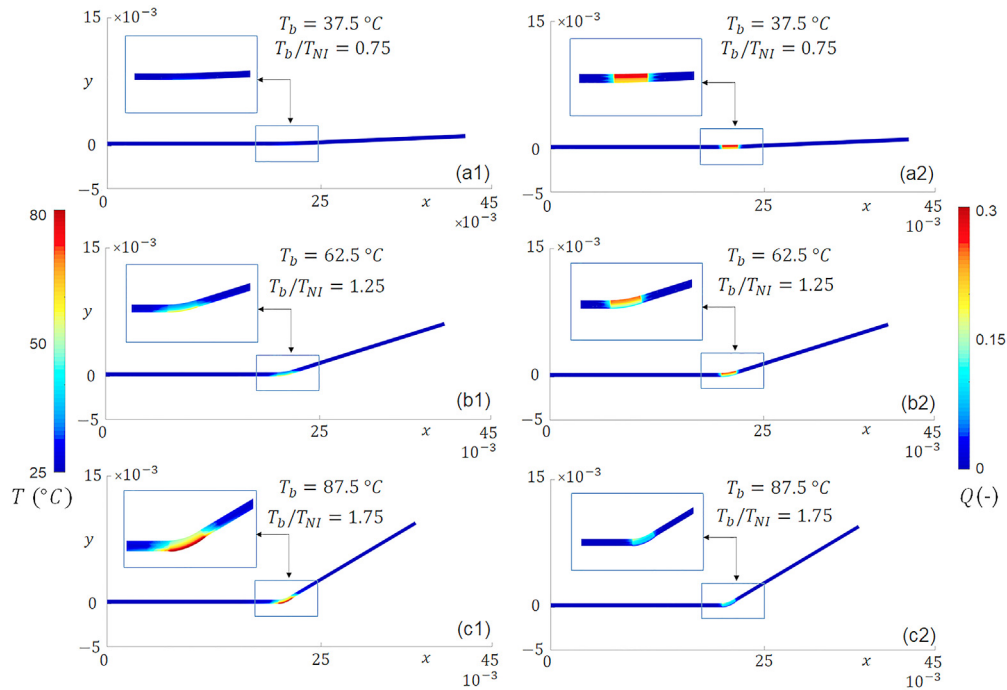

Fig. 10. Temperature pattern (left column) within the LT_{NI} LCE hinge at different dimensionless temperatures, $T_b/T_{NI} = 0.75$ (a1), $T_b/T_{NI} = 1.25$ (b1), $T_b/T_{NI} = 1.75$ (c1). Corresponding order parameter patterns at the same dimensionless temperatures (right column). A temperature increase corresponds to a decrease of the order parameter which induces the rotation angle θ to raise.

is known, we can determine the deformation taking place in the two layers of the element and evaluate the radius of curvature and the arising rotation angle θ (see Fig. 4a).

A temperature dependence similar to that adopted for the nematic order $Q(T)$ (see Secttion 3.1) is adopted here for the term a_h, which is assumed to range between a minimum value of 1.001 (at room temperature) and a maximum one of 1.15 (above the T_{NI} temperature).

We compare the results from the statistical mechanics model and the theoretical ones obtained from the plate model from Agostiniani and DeSimone (2017) to the LT_{NI} LCE experiments first. The rotation vs LCE bottom temperature is displayed in Fig. 7a, while the strain measured at the top point of the central vertical cross section of the LCE element vs temperature is represented in Fig. 7b. We note that in experiments, the absolute value of the transverse deformation is smaller than of the longitudinal deformation because the material is incompressible. This difference is not captured as clearly in the numerical results due to the adoption of a 2D plane stress model. The deformations parallel and perpen-
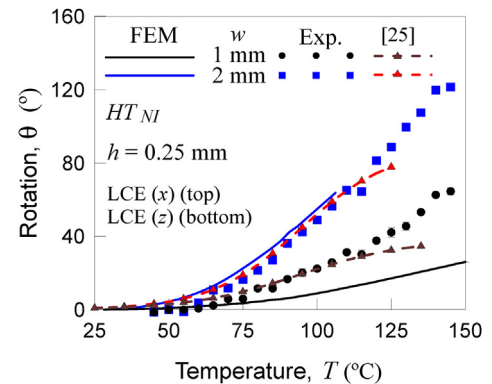
Fig. 11. Rotation angle vs temperature (measured at the bottom surface of the LCE element) for the HT_{NI} LCE hinge with thickness $h = 0.25$ mm and width $w = 1$ and 2 mm. Comparison between the FE results, experimental (Kotikian et al., 2019) and theoretical (Agostiniani and DeSimone, 2017) data are shown.
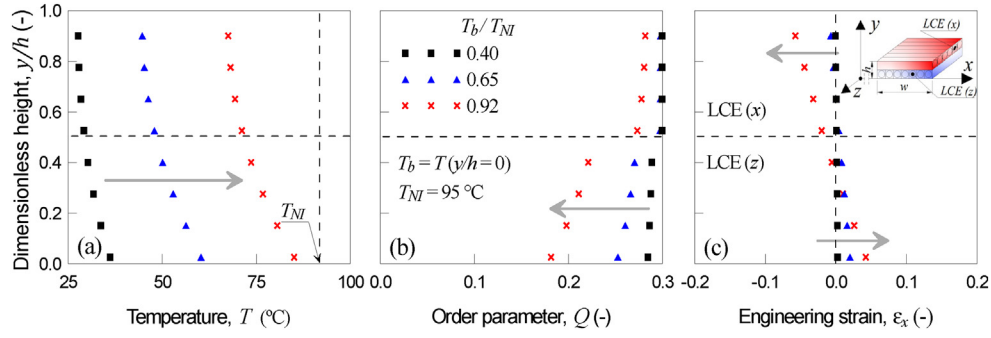
Fig. 12. Profiles of the temperature (a), of the order parameter Q (b) and of the longitudinal strain ε_x (c) along the HT_{NI} LCE hinge centerline vertical section ($h = 0.25$ mm, $w = 2$ mm) provided by the present model. Different values of the dimensionless temperature T_b/T_{ni} are considered, namely 0.40, 0.65 and 0.92.
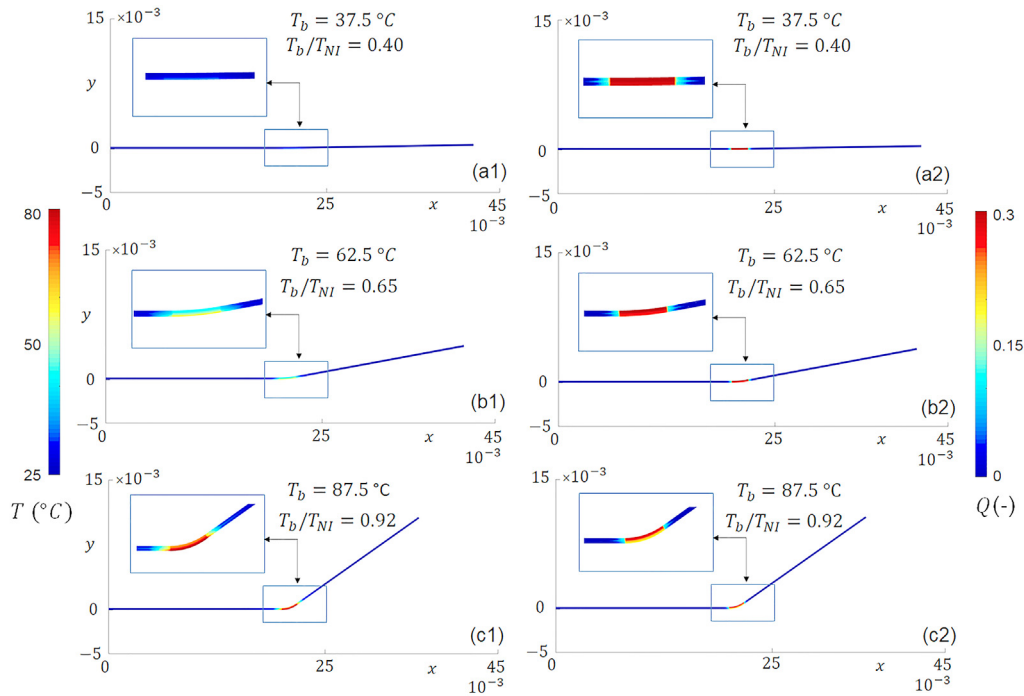
Fig. 13. Temperature pattern (left column) within the HT_{NI} LCE hinge at different dimensionless temperatures, $T_b/T_{NI} = 0.40$ (a1), $T_b/T_{NI} = 0.65$ (b1), $T_b/T_{NI} = 0.92$ (c1). Corresponding order parameter patterns at the same dimensionless temperatures (right column). A temperature increase corresponds to a decrease of the order parameter which induces the bending angle to increase.

dicular to the nematic direction obtained numerically have been reported for three points placed at different positions along the vertical line: point A at $\eta = 2y'/h = 0.8$, point B at $\eta = 0.55$ and point C at $\eta = 0.3$.

The rotation angle as a function of temperature $\theta(T)$ provided by the model underestimates the rotation measured experimentally, while it fits well with the theoretical model. We note that the initial angle θ of the specimen at room temperature is negative due to the residual stresses that arise during 3D printing. For sake of comparison, the numerical values of the rotation have been shifted so that they start from the same initial value. The discrepancy between simulations and experiments in this case may be due to the presence of residual stresses in the as-fabricated materials, which are not accounted for in the model. On the other hand, the strains measured parallel to the initial mesogen alignment (x direction) and the one evaluated perpendicular to that direction (y) follow reasonably the measured deformations (Fig. 7b) for a monolayer LCE specimen.

The rotation angle as a function of temperature and the parallel and normal strains for two different geometries of these LCE hinges

are reported in Fig. 8a and b, respectively. There is little difference between the folding angles obtained for each LCE geometry.

The distributions of temperature, nematic order, and strain ε_x along the vertical centerline of a LT_{NI} LCE element ($h = 0.25$ mm and $w = 1$ mm), according to results from the FE implementation of the model, are reported in Fig. 9 for three different values of the bottom boundary temperature T_b (measured at $y = 0$) to transition temperature T_{NI} ratio. Increasing temperature causes the order parameter to decrease. Consequently, the top layer of the LCE element contracts in the x-direction and the bottom layer expands, which induces bending.

Fig. 10 illustrates the contour map of the temperature T (left column) and of the order parameter Q (right column) for an element with $h = 0.5$ mm, $w = 2$ mm, and the same above-mentioned T_b/T_{NI} ratios. In the simulation, the nematic order quickly reduces from its initial value, tending toward zero more rapidly in the bottom part of the LCE directly exposed to the heat source.

Fig. 11 shows the rotation computed by the proposed model as a function of the LCE's bottom boundary temperature for the HT_{NI}

case. The two analyzed geometries have $h = 0.25$ mm, but differ in having $w = 1$ and 2 mm. Experimental results from Kotikian et al. (2019) as well as theoretical results from Agostiniani and DeSimone (2017) are also reported for comparison. There is very good agreement for the widest LCE hinge while the rotation evaluated by the model slightly underestimates the behavior of the narrower sample at high temperatures.

Fig. 12 shows the distributions of the temperature, nematic order, and strain ε_x along the vertical centerline of an HT_{NI} LCE element for three different values of the bottom boundary temperature (T_b) to transition temperature (T_{NI}) ratio. Here, $h = 0.25$ mm and $w = 2$ mm. As with the LT_{NI} LCE, a temperature increase leads to a decrease in the order parameter and causes bending, though not as pronounced as in the case of the LT_{NI} LCE.

Fig. 13 shows the contour map of the temperature T (left column) and of the order parameter Q (right column) for the element with $h = 0.25$ mm, $w = 2$ mm and for some values of the T_b/T_{NI} ratios. Again, the nematic order quickly reduces from its initial value of 0.3 to zero more rapidly in the bottom part of the LCE directly exposed to the heat source, leading to an expansion in the direction transversal to the initial nematic orientation.

Hence, we have shown that a statistical mechanics approach can be effective in modeling the bending behavior of LCE bilayer actuators. There is good correspondence between results from the model with prior theoretical work (Agostiniani and DeSimone, 2017) and with experiments, except in the case where the residual stresses that arise from the LT_{NI} LCE printing process are significant (Kotikian et al., 2019).

6. Conclusions

In this paper, we presented a mechanical model of liquid crystal elastomers (LCEs) that undergo changes in nematic order in response to thermal stimulus. Starting from a statistical-based micromechanical model that captures the evolution of the network chain distribution tensor, we arrive at a mesoscale description of the mechanical response of LCE under an external heat stimulus. The parameters involved can be tuned easily, and they all have a clear physical meaning. The microscale model allows us to describe the response of LCE elements at the continuum scale (through proper upscaling) and is suitable to be implemented in a generic computational framework. We conducted several parametric analyses and the results provided by the model were compared with experimental and theoretical results from the literature. The micromechanical approach is a promising tool for the analysis and design of LCE actuators. A better understanding of the impact on nematic arrangement and material properties (prescribed using modern 3D printing technologies, for example) can lead to structures whose responses to environmental stimuli are precisely tuned according to the application of interest.

Declaration of Competing Interest

The authors declare that they have no known competing financial interests or personal relationships that could have appeared to influence the work reported in this paper.

Acknowledgements

References

Agostiniani, V., DeSimone, A., 2017. Rigorous derivation of active plate models for thin sheets of nematic elastomers 1081286517699991 Math. Mech. Solids. https://doi.org/10.1177/1081286517699991.

Agostiniani, V., DeSimone, A., 2017. Dimension reduction via Γ-convergence for soft active materials. Meccanica 52 (14), 3457–3470. https://doi.org/10.1007/s11012-017-0630-4.

Aguilar, M.R., Elvira, C., Gallardo, A., Vázquez, B., Román, J.S., 2007. Smart polymers and their applications as biomaterials. Top. Tissue Eng. 3 (6).

Aharoni, H., Sharon, E., Kupferman, R., 2014. Geometry of thin nematic elastomer sheets. Phys. Rev. Lett. 113, (25). https://doi.org/10.1103/PhysRevLett.113.257801 257801.

Aharoni, H., Xia, Y., Zhang, X., Kamien, R.D., Yang, S., 2018. Universal inverse design of surfaces with thin nematic elastomer sheets. Proc. Natl. Acad. Sci. 115 (28), 7206–7211. https://doi.org/10.1073/pnas.1804702115.

Ambulo, C.P., Burroughs, J.J., Boothby, J.M., Kim, H., Shankar, M.R., Ware, T.H., 2017. Four-dimensional printing of liquid crystal elastomers. ACS Appl. Mater. Interfaces 9 (42), 37332–37339. https://doi.org/10.1021/acsami.7b11851.

Anderson, D.R., 1966. Thermal conductivity of polymers. Chem. Rev. 66 (6), 677–690. https://doi.org/10.1021/cr60244a004.

Biggins, J.S., Warner, M., Bhattacharya, K., 2009. Supersoft elasticity in polydomain nematic elastomers. Phys. Rev. Lett. 103,. https://doi.org/10.1103/PhysRevLett.103.037802 037802.

Biggins, J.S., Warner, M., Bhattacharya, K., 2012. Elasticity of polydomain liquid crystal elastomers. J. Mech. Phys. Solids 60 (4), 573–590. https://doi.org/10.1016/j.jmps.2012.01.008.

Bladon, P., Terentjev, E.M., Warner, M., 1993. Transitions and instabilities in liquid crystal elastomers. Phys. Rev. E 47 (6), R3838. https://doi.org/10.1103/PhysRevE.47.R3838.

Bladon, P., Terentjev, E.M., Warner, M., 1994. Deformation–induced orientational transitions in liquid crystals elastomer. J. Phys. II 4 (1), 75–91. https://doi.org/10.1051/jp2:1994100.

Brighenti, R., Artoni, F., Cosma, M.P., 2019. Mechanics of materials with embedded unstable molecules. Int. J. Solids Struct. 162, 21–35. https://doi.org/10.1016/j.ijsolstr.2018.11.022.

Cao, Z.Q., Wang, G.J., 2016. Multi-stimuli-responsive polymer materials: particles, films, and bulk gels. Chem. Rec. 16 (3), 1398–1435. https://doi.org/10.1002/tcr.201500281.

Choy, C.L., 1977. Thermal conductivity of polymers. Polymer 18 (10), 984–1004. https://doi.org/10.1016/0032-3861(77)90002-7.

Cirak, F., Long, Q., Bhattacharya, K., Warner, M., 2014. Computational analysis of liquid crystalline elastomer membranes: Changing Gaussian curvature without stretch energy. Int. J. Solids Struct. 51 (1), 144–153. https://doi.org/10.1016/j.ijsolstr.2013.09.019.

Clarke, S.M., Hotta, A., Tajbakhsh, A.R., Terentjev, E.M., 2001. Effect of crosslinker geometry on equilibrium thermal and mechanical properties of nematic elastomers. Phys. Rev. E 64, (6). https://doi.org/10.1103/PhysRevE.64.061702 061702.

Davidson, E.C., Kotikian, A., Li, S., Aizenberg, J., Lewis, J.A., 2020. 3D printable and reconfigurable liquid crystal elastomers with light-induced shape memory via dynamic bond exchange. Adv. Mater. 32, 1905682. https://doi.org/10.1002/adma.201905682.

De Gennes, P.G., Prost, J., 1993. The Physics of Liquid Crystals. Oxford University Press.

DeSimone, A., 2010. Nematic elastomers: modelling, analysis, and numerical simulations. In: Poly-, Quasi-and Rank-One Convexity in Applied Mechanics. Springer, Vienna, pp. 241–264.

Doi, M., 1996. Introduction to Polymer Physics. Oxford University Press.

Ennis, R., Malacarne, L.C., Palffy-Muhoray, P., Shelley, M., 2006. Nonlocal model for nematic liquid-crystal elastomers. Phys. Rev. E 74, (6). https://doi.org/10.1103/PhysRevE.74.061802 061802.

Ericksen, J.L., 1961. Conservation laws for liquid crystals. Trans. Soc. Rheol. 5, 23–34. https://doi.org/10.1122/1.548883.

Finkelmann, H., Greve, A., Warner, M., 2001. The elastic anisotropy of nematic elastomers. Eur. Phys. J. E 5 (3), 281–293. https://doi.org/10.1007/s101890170060.

Frank, E.C., 1958. On the theory of liquid crystals. Discuss. Faraday Soc. 25, 19–28. https://doi.org/10.1039/DF9582500019.

Fu, X., Hosta-Rigau, L., Chandrawati, R., Cui, J., 2018. Multi-stimuli-responsive polymer particles, films, and hydrogels for drug delivery. Chem. 4, 2084–2107. https://doi.org/10.1016/j.chempr.2018.07.002.

Fu, C., Xu, F., Huo, Y., 2018. Photo-controlled patterned wrinkling of liquid crystalline polymer films on compliant substrates. Int. J. Solids Struct. 132, 264–277. https://doi.org/10.1016/j.ijsolstr.2017.10.018.

Gō, N., Scheraga, H.A., 1976. On the use of classical statistical mechanics in the treatment of polymer chain conformation. Macromolecules 9 (4), 535–542. https://doi.org/10.1021/ma60052a001.

Griniasty, I., Aharoni, H., Efrati, E., 2019. Curved geometries from planar director fields: Solving the two-dimensional inverse problem. Phys. Rev. Lett. 123, (12). https://doi.org/10.1103/PhysRevLett.123.127801 127801.

Guin, T., Settle, M.J., Kowalski, B.A., Auguste, A.D., Beblo, R.V., Reich, G.W., White, T.J., 2018. Layered liquid crystal elastomer actuators. Nat. Commun. 9 (1), 1–7. https://doi.org/10.1038/s41467-018-04911-4.

Guragain, S., Bastakoti, B.P., Malgras, V., Nakashima, K., Yamauchi, Y., 2015. Multi-stimuli-responsive polymeric materials. Chem.–A Eur. J. 21 (38), 13164–13174. https://doi.org/10.1002/chem.201501101.

Hänggi, P., Talkner, P., Borkovec, M., 1990. Reaction-rate theory: fifty years after Kramers. Rev. Modern Phys. 62 (2), 251–341. https://doi.org/10.1103/RevModPhys.62.251.

Jin, L., Zeng, Z., Huo, Y., 2010. Thermomechanical modeling of the thermo-order–mechanical coupling behaviors in liquid crystal elastomers. J. Mech. Phys. Solids 58 (11), 1907–1927. https://doi.org/10.1016/j.jmps.2010.07.019.

Jin, L., Lin, Y., Huo, Y., 2011. A large deflection light-induced bending model for liquid crystal elastomers under uniform or non-uniform illumination. Int. J. Solids Struct. 48 (22–23), 3232–3242. https://doi.org/10.1016/j.ijsolstr.2011.07.015.

Kim, H., Gibson, J., Maeng, J., Saed, M.O., Pimentel, K., Rihani, R.T., Pancrazio, J.J., Georgakopoulos, S.V., Ware, T.H., 2019. Responsive, 3D electronics enabled by liquid crystal elastomer substrates. ACS Appl. Mater. Interfaces 11 (21), 19506–19513. https://doi.org/10.1021/acsami.9b04189.

Kotikian, A., Truby, R.L., Boley, J.W., White, T.J., Lewis, J.A., 2018. 3D printing of liquid crystal elastomeric actuators with spatially programed nematic order. Adv. Mater. 30 (10), 1706164. https://doi.org/10.1002/adma.201706164.

Kotikian, A., McMahan, C., Davidson, E.C., Muhammad, J.M., Weeks, R.D., Daraio, C., Lewis, J.A., 2019. Untethered soft robotic matter with passive control of shape morphing and propulsion. Sci. Robotics 4. https://doi.org/10.1126/scirobotics.aax7044.

Kowalski, B.A., Mostajeran, C., Godman, N.P., Warner, M., White, T.J., 2018. Curvature by design and on demand in liquid crystal elastomers. Phys. Rev. E 97, (1). https://doi.org/10.1103/PhysRevE.97.012504 012504.

Kuhn, W., Grün, F., 1942. Beziehungen zwischen elastischen konstanten und dehnnungsdoppelbrechung hochelastischer stoffe. Colloid Polym. Sci. 101 (3), 248–271. https://doi.org/10.1007/BF01793684.

Leslie, E.M., 1968. Some constitutive equations for liquid crystals. Arch. Rat. Mech. Anal. 28, 265–283. https://doi.org/10.1007/BF00251810.

Leslie, F.M., 1992. Continuum theory for nematic liquid crystals. Continuum Mech. Thermodyn. 4 (3), 167–175. https://doi.org/10.1007/BF01130288.

Lifson, S., 1964. Partition functions of linear-chain molecules. J. Chem. Phys. 40 (12), 3705–3710. https://doi.org/10.1063/1.1725077.

Maier, W., Saupe, A.Z., 1958. Eine einfache molekulare Theorie des nematischen kristallinflüssigen Zustandes. Naturforsch 13a, 564–566. https://doi.org/10.1515/zna-1958-0716.

Mihai, L.A., Goriely, A., 2020. A plate theory for nematic liquid crystalline solids. J. Mech. Phys. Solids 104101. https://doi.org/10.1016/j.jmps.2020.104101.

Mitchell, G.R., Davis, F.J., Guo, W., 1993. Strain-induced transitions in liquid-crystal elastomers. Phys. Rev. Lett. 71 (18), 2947. https://doi.org/10.1103/PhysRevLett.71.2947.

Modes, C.D., Bhattacharya, K., Warner, M., 2011. Gaussian curvature from flat elastica sheets. Proc. R. Soc. A: Math., Phys. Eng. Sci. 467 (2128), 1121–1140. https://doi.org/10.1098/rspa.2010.0352.

Mostajeran, C., 2015. Curvature generation in nematic surfaces. Phys. Rev. E 91, (6). https://doi.org/10.1103/PhysRevE.91.062405 062405.

Ohm, C., Brehmer, M., Zentel, R., 2012. Applications of liquid crystalline elastomers. In: Liquid Crystal Elastomers: Materials and Applications. Springer, Berlin, Heidelberg, pp. 49–93.

Oseen, W.C., 1933. The theory of liquid crystals. Trans. Faraday Soc. 29, 883–899. https://doi.org/10.1039/TF9332900883.

Plucinsky, P., Lemm, M., Bhattacharya, K., 2016. Programming complex shapes in thin nematic elastomer and glass sheets. Phys. Rev. E 94, (1). https://doi.org/10.1103/PhysRevE.94.010701 010701.

Rubinstein, M., Colby, R.H., 2003. Polymer Physics. Oxford University Press.

Saeva, F.D., 1979. Liquid Crystals. The Fourth State of Matter. CRC Press. ISBN-10: 0824768132.

Schattling, P., Jochum, F.D., Theato, P., 2014. Multi-stimuli responsive polymers–the all-in-one talents. Polym. Chem. 5 (1), 25–36. https://doi.org/10.1039/C3PY00880K.

Shahinpoor, M., Schneider, H.J., 2008. Intelligent materials. R. Soc. Chem. https://doi.org/10.1039/9781847558008.

Silberstein, M.N., Min, K., Cremar, L.D., Degen, C.M., Martinez, T.J., Aluru, N.R., White, S.R., Sottos, N.R., 2013. Modeling mechanophore activation within a crosslinked glassy matrix. J. Appl. Phys. 114, (2). https://doi.org/10.1063/1.4812581 023504.

Stephen, M.J., Straley, J.P., 1974. Physics of liquid crystals. Rev. Mod. Phys. 46 (4), 617. https://doi.org/10.1103/RevModPhys.46.617.

Surjadi, J.U., Gao, L., Du, H., Li, X., Xiong, X., Fang, N.X., Lu, Y., 2019. Mechanical metamaterials and their engineering applications. Adv. Eng. Mater. 21 (3), 1800864. https://doi.org/10.1002/adem.201800864.

Terentjev, E.M., Warner, M., 2001. Linear hydrodynamics and viscoelasticity of nematic elastomers. Eur. Phys. J. E 4 (3), 343–353. https://doi.org/10.1007/s101890170117.

Vernerey, F.J., Long, R., Brighenti, R., 2017. A statistically-based continuum theory for polymers with transient networks. J. Mech. Phys. Solids 107, 1–20. https://doi.org/10.1016/j.jmps.2017.05.016.

Ware, T.H., McConney, M.E., Wie, J.J., Tondiglia, V.P., White, T.J., 2015. Voxelated liquid crystal elastomers. Science 347 (6225), 982–984. https://doi.org/10.1126/science.1261019.

Warner, M., Terentjev, E.M., 2007. Liquid Crystal Elastomers. Oxford University Press.

Warner, M., Gelling, K.P., Vilgis, T.A., 1988. Theory of nematic networks. J. Chem. Phys. 88 (6), 4008–4013. https://doi.org/10.1063/1.453852.

Waters, J.T., Li, S., Yao, Y., Lerch, M.M., Aizenberg, M., Aizenberg, J., Balazs, A.C., 2020. Twist again: Dynamically and reversibly controllable chirality in liquid crystalline elastomer microposts. Sci. Adv. 6 (13). https://doi.org/10.1126/sciadv.aay5349. eaay5349.

Wen, J., 2007. Heat capacities of polymers. In: Physical Properties of Polymers Handbook. Springer, New York, NY, pp. 145–154.

Zhang, Y., Xuan, C., Jiang, Y., Huo, Y., 2019. Continuum mechanical modeling of liquid crystal elastomers as dissipative ordered solids. J. Mech. Phys. Solids 126, 285–303. https://doi.org/10.1016/j.jmps.2019.02.018.